Title: *Instability of flood embankments due to pore water pressure build-up at the toe: lesson learned from the Adige river case study.*

Authors:

Alessia Amabile (ORCID 0000-0001-6682-1926) – corresponding author

Email: alessia.amabile@strath.ac.uk

Annarita Pozzato

Email: annarita.pozzato@strath.ac.uk

Alessandro Tarantino (ORCID 0000-0001-6690-748X)

Email: alessandro.tarantino@strath.ac.uk

Affiliation for all authors: University of Strathclyde, Glasgow, UK

Address: Civil and Environmental Engineering Department,

75 Montrose Street - Glasgow G1 1XJ, Scotland, UK

Abstract

The paper presents the case study of the Adige river embankment, a segment of which experienced instability of the landside slope due to the development of uplift pressures. Soil profile and hydro-mechanical properties of the embankment and foundation materials have been assessed via site investigation, laboratory testing, and field monitoring for two cross sections, within and outside the failure segment respectively. The hydro-mechanical model developed thereof was first validated against its ability to reproduce the probability of failure for the two sections with a FOSM-based approach. Comparison of water flow regimes between the two sections was then used to highlight the importance of the hydraulic properties of the material on the landside for the development of uplift pressures at the toe of the embankment. The lesson learnt from this case study is that the hydraulic response of the ground on the landside may play a critical role on the stability of flood embankments and its characterisation should therefore not be overlooked when planning site investigation.

Keywords

flood embankments; slope stability; uplift pressure; landside; case study

Introduction

Flood embankments are essential structures in flood defence systems and their failure can lead to devastating consequences. One of the most critical failure mechanisms is represented by the instability of the landside slope triggered by the development of high uplift pressures at the toe of the embankment (Phoon, 2008), often accompanied by the formation of sand boils (CIRIA; French Ministry of Ecology; USACE, 2013). This is frequently the case when embankments are built on top of foundation layers having significantly higher hydraulic conductivity.

The development of uplift pressure at the toe of the embankment can lead to failure by triggering two different failure mechanisms; one is the piping process caused by seepage and internal erosion, while the other is the instability caused by the increase of pore water pressure and consequent decrease of shear strength of the soil (Dyer, 2004). The main failure mechanism depends on whether the embankment is built directly on top of a permeable foundation soil, or an intermediate impermeable layer is interposed between the permeable subsoil and the embankment; in the first case, piping tends to be the prevailing failure mechanism, while in the second case instability triggered by uplift pressures tends to be the dominant one (Hird, et al., 1978).

In the literature there are only a few case studies documenting the development of uplift pressure as the primary cause of instability of embankments. The first case study is found in Cooling and Marsland (1953), who showed that the failure occurred in the embankment at Dartfort Creek in 1953 was caused by the development of high pore water pressure in the underlying layers of permeable sandy gravel that lead to a decrease in shear strength and therefore instability of the landside slope. Uplift induced failure is also estimated to be the most likely failure mechanism in the Western region of the Netherlands, where many flood embankments are built on top of a very permeable sand layer (Bauduin, et al., 1989; Van, et al., 2005). Although this kind of stratigraphy is not uncommon, Van et al. (2005) suggest that one of the reasons why only two case studies are reported in the literature is that this failure mechanism has not been recognised in other occasions, either because of the damage resulting from the failure or because of unawareness.

An exception in more recent years is represented by the catastrophic breach on the North London Canal in New Orleans during Hurricane Katrina in 2005, which resulted in the flooding of the most densely populated area of New Orleans. The instability was caused by uplift pressures at the toe of the embankment, which was built over a foundation layer of loose sand (Seed, et al., 2008). While Kanning et al. (2008) pointed out that there is still some uncertainty about the reasons why the failure occurred exactly at that location and not in any other sections with a similar soil profile, Seed et al. (2008) concluded that the only explanation was to be found in the subtle difference in soil profile in the foundation layer at the toe of the embankment. In the failed section, the interface between the layers had a gentle slope and was almost horizontal, while on the opposite bank, the presence of a steeper interface between the layers altered the shape of the slip surface and enhanced the stability of the embankment.

The aim of this work is to show that the high contrast in hydraulic conductivity between a pervious foundation layer and a relatively impervious embankment material does not represent per se a critical condition for the development of uplift pressures and to highlight the key role played by the soil profile on the landside even outside the footprint of the embankment.

This paper presents a case study associated with a segment of the Adige River embankment subject to instability during a flood in 1981 for the first time ever since construction, between 1860 and 1890 (Werth, 2003). This segment experienced instability with a failure mechanism on the landside (Pozzato, et al., 2014), likely associated with uplift pressures as boiling is often observed during intense flood events. Instability was characterised by the formation of a scarp, but the embankment did not experience a full collapse. As a result, the materials and soil profile to date are exactly the same as at the time of failure. This offers the unique chance to characterise the soil profile and hydro-mechanical properties of the embankment and its foundation as they were at the time of failure. This is rarely the case as instability is often accompanied by a breach with the embankment and the foundation layers swept away, making soil profile and material characterisation impossible to reconstruct a posteriori. Field and laboratory testing was carried out to characterise stratigraphy and soil's hydro-mechanical properties for two cross sections, one within and one outside the failure segment. The hydro-mechanical model was first validated against its capability to reproduce realistic probability of failure within and outside the failure segment and then used to highlight critical aspects of the failure mechanism.

The case-study

The embankments on the Adige River[1] were built at the end of 19th century to straighten the river path. The traces of the ancient meanders are still visible along the alluvial valley and are easily recognisable from aerial photographs and satellite images (Angelucci, 2013). These resources can be coupled with historical cartography to reconstruct the ancient meandering path of the river (Fig. 1).

During an intense flood event in July 1981, a 230 m segment of the embankment near the village of San Floriano experienced instability and a 50 cm deep scarp was observed on the crest of the embankment[2]. The probability of failure has been assessed for this segment as well as for a section in the south outside the failure segment ('stable' in Fig. 1).

Soil profile

Soil profile has been inferred from boreholes and Dynamic Probing Heavy (DPH) tests from the crest at different locations along a 500 m segment, which includes the failure segment and the stable zone south of the failure segment. Layer boundaries inferred from visual inspection

[1] Northern Italy in Figure S1.
[2] Picture of the scarp in Figure S2.

of core samples and DPH blow number are shown as diamonds and circles respectively in Fig. 2. The soil profile was then cross-checked via the grain-size distribution (GSD) of samples taken from the identified soil horizons (black rectangles in Fig. 2).

The body of the embankment is made of two different layers. The upper layer is a gravelly shell, whereas the core of the embankment is a brown sandy silt. The thickness of the embankment core layer is fairly constant (~6 m) along the 500 m segment. The thickness of the gravelly shell is slightly larger in the area located north of the failure zone, closer to San Floriano Bridge, but it is fairly constant (~1.1 m) in the area of the failure segment and outside the failure segment in the south.

Two layers form the embankment foundation. The first layer is a brown-grey sandy material, with significant coarse fraction and rounded particles. This material has alluvial origin and corresponds to the ancient riverbed where the Adige River flowed before being straightened. This material is also encountered outside the ancient riverbed projection as derived from aerial photographs and historical maps (Fig. 1). This is because the alluvial deposit extends beyond the ancient riverbed on the inner side of the meander due to deposition phenomena. The deep foundation layer is a dark grey sandy deposit, with local lenses of finer material. It constitutes the glacial lacustrine deposit where the Adige River formed its meandering path.

The two cross sections examined in this study are located at chainage km 122.25 (within the failure segment) and at chainage km 122.42 (outside the failure segment). After the failures observed in 1981 the entire segment of embankment has been reinforced by a berm on the landside slope[3] which has not been included in the geotechnical model in this study.

Only two boreholes, B131 and B132 for the sections within and outside the failure segment respectively[3], have been drilled on the landside at the toe of the embankment down to 4m.

[3] Topography in Figure S3.

Additional information was therefore required to characterise the soil profile on the landside. Investigation was carried out using EM profiling based on Slingram method (Nabighian, 1992) using the device GEM2 (GEOPHEX USA) along the toe of the embankment. Results are shown in Fig. 3. The sharp local anomalies of resistivity (chainage km 122.19, 122.28, 122.35) are associated with the presence of artificial metal objects on the surface. Within the failure segment, apparent resistivity is essentially constant with a slightly increasing trend from chainage km 122.24 to km 122.39. Outside the failure segment the resistivity increases, more markedly from chainage km 122.41. This is associated with the appearance of the sandy alluvial deposit generated by the ancient river, which is close to the embankment in the south section. The alluvial deposit on the landside therefore appears in the south but not in the failure segment, as reflected in the soil profile for the two cross-sections (in Fig. 4).

Grain size distributions for the identified materials are shown in Fig. 5. The embankment core is fairly homogeneous within and outside the failure segment. The alluvial material and the lacustrine material show larger variability along the longitudinal profile (Fig. 5b).

The grain size distribution of the sample collected at a depth of 3.5m from the only borehole on the landside in the section outside the failure segment (B132B) is consistent with the grain size distribution of the alluvial material. This confirms that the alluvial deposit extends beyond the toe of the embankment in the section located south of the failure segment.

Hydro-mechanical characterisation

Laboratory testing was carried out to investigate shear strength, saturated hydraulic conductivity, and water retention behaviour of the embankment material. Cell piezometers and tensiometers were installed in the zone below and above phreatic surface respectively and their measurements were used to characterise the hydraulic properties of the embankment and the shallow foundation layer by inverse analysis of hydraulic flow.

Deterministic hydraulic characterisation

Water retention behaviour of embankment material

Water retention behaviour of the embankment material was determined from loose samples reconstituted in the laboratory by compaction at target dry density of 1.53 g/cm^3 consistent with the estimated field value. The density index of the embankment material was first estimated based on SPT and DPH tests (EN 1997-2, 2007). The density index was found to be in the range 0.19-0.32. Assuming a minimum and a maximum void ratio $e_{\min}$=0.30 and $e_{\max}$=0.90 (Lambe & Whitman, 1969), the dry density was therefore estimated to be in the range 1.50-1.57 g/cm^3. Specimens 100 mm diameter and 100 mm high were compacted to gravimetric water contents ranging from 9% to 21%. After moisture equilibration overnight, matric suction was measured using a High-Capacity Tensiometer (Tarantino & Mongiovì, 2003). Water retention data points of compacted samples can be associated with the main wetting curve (Tarantino & Tombolato, 2005), which is reasonably representing water retention behaviour for infiltration associated with the flood.

The experimental data points have been fitted with van Genuchten model for water retention (van Genuchten, 1980). The effective saturation S_e is defined by Eq. 1:

$$S_e = \frac{\theta - \theta_{res}}{\theta_{sat} - \theta_{res}} = \frac{1}{(1 + (\alpha s)^n)^m} \qquad \textbf{Eq. 1}$$

where s is the suction, θ, θ_{sat} and θ_{res} are the current, saturated, and residual volumetric water contents respectively, α and n are soil parameters (α=0.07 kPa^{-1} and n=1.438) and $m = 1\text{-}1/n$. The relative hydraulic conductivity was derived from S_e as per Eq. 2 (van Genuchten, 1980).

$$k_{rel} = S_e^{-0.5}\left(1 - \left(1 - S_e^{\frac{1}{m}}\right)^m\right)^2 \qquad \textbf{Eq. 2}$$

Saturated hydraulic conductivity of foundation layers via laboratory testing

Two specimens 80 mm diameter and 20 mm high were cut from samples taken from the alluvial deposit and lacustrine deposit at the depths of 7.3-7.7 and 12.7-13.00 respectively (Borehole B551). The specimens were consolidated in an oedometer to 160kPa and 250 kPa for the 7.3-7.7 and 12.7-13.00 samples respectively to reproduce field effective stress (Aldegheri, 2009).

Constant head hydraulic conductivity tests were carried out by connecting the base of the oedometer to a water reservoir placed on a balance to measure water flow rate. The values obtained for the saturated hydraulic conductivity were $8 \cdot 10^{-6}$ m/s and $4 \cdot 10^{-8}$ m/s for alluvial and lacustrine deposit respectively. The values were not considered representative of the field hydraulic conductivity in the sense that differences of 1-2 order of magnitude are generally observed between laboratory and field values (Herzog & Morse, 1986). Nonetheless, the ratio between these two laboratory values was assumed to be representative of the same ratio of field values.

Saturated hydraulic conductivity of embankment and upper foundation via inverse analysis of piezometer and tensiometer data

A monitoring system has been installed at the section outside the failure segment consisting of i) 6 pressure transducers (B1-MOD level transducer from Tecnopenta) installed via bayonet fitting at the bottom of standpipe piezometers to measure pore-water pressure below the phreatic surface mainly in the alluvial deposit and ii) 5 tensiometers (T8 tensiometer from UMS) to measure suction above the phreatic surface (Fig. 4).

The calibration of the TecnoPenta pressure transducers was verified in the field by moving the pressure transducer at different locations in the standpipe piezometers (filled with water once the piezometer was removed from its bayonet fitting). The calibration curve of the UMS tensiometers was verified in the field by submerging the porous tip into a water-filled container and imposing vacuum via a hand-operated pump.

Measurements recorded by the instruments were used to characterise the saturated hydraulic conductivity of the embankment and the alluvial deposit by inverse analysis. The time selected for the inverse analysis is a two-week window in summer 2016, where the Adige River recorded its highest level since the installation of the instruments[4].

Measurements by the shallow tensiometer T6, closer to the ground surface, were clearly affected by the rainfall, whereas measurements by the intermediate and deep tensiometers were not[5]. Atmospheric boundary conditions on the crest of the embankment did not have a significant effect on the seepage in the embankment core below shallow depths. At the same time, intermediate and deeper tensiometers clearly responded to the fluctuation of the river level, which was considered as the hydraulic boundary condition in the inverse analysis.

The saturated hydraulic conductivities of the embankment and the alluvial deposit were selected to allow for the best matching between simulated and observed data. In lack of data, the ratio between the hydraulic conductivities in vertical and horizontal direction has been assumed equal to $k_V/k_H = 0.1$ for the foundation layers (Lancellotta, 2009).

The comparison between simulated and measured pore-water pressure values was considered satisfactory. The maximum difference between measured and simulated values was less than 4 kPa for the piezometers and less than 3 kPa for the tensiometers. A sample showing results for two of the tensiometers and one piezometer is reported in Fig. 6[6]. The values of saturated hydraulic conductivity derived from the inverse analysis are $2{\cdot}10^{-6}$ m/s and $4{\cdot}10^{-3}$ m/s for the embankment material and alluvial deposit respectively. It is worth observing that the saturated hydraulic conductivity for the alluvial deposit material derived from the inverse analysis is

[4] River level variations in Figure S4.
[5] Measurements in Figure S5.
[6] Full set of data in Figure S6.

greater than the one measured in the laboratory tests by about two orders of magnitude, which is a difference typically encountered when comparing laboratory and field measurements of hydraulic conductivity.

Deterministic shear strength characterisation

Shear strength behaviour of the embankment material was determined on two sets of specimens. Two specimens from within the failure segment (B551, depth 4.20 - 4.80m) were reconstituted from slurry. After flooding the shear box container with water to submerge the sample, the two specimens 20 mm high were initially consolidated to a maximum vertical stress of 75 kPa and 150 kPa respectively. The target vertical stress was attained in stages and the specimens were allowed to consolidate fully under each vertical stress increment. The time required to achieve primary consolidation was always less than 1 min. Specimens were sheared at shear displacement rate of 2mm/h. This rate was sufficiently slow to ensure shear under drained conditions (Aldegheri, 2009). Both specimens showed a monotonic increase in shear strength until the ultimate state with compressive behaviour.

Two specimens from outside the failure segment (B739, depth 3.0-3.3 m) were compacted into the shearbox to vertical stress of 200 kPa and water content of 18% and 21% respectively to achieve a target dry density similar to the specimens prepared for the water retention behaviour. Specimens were then unloaded to 100 kPa and 50 kPa vertical stress respectively to simulate field stress conditions. Afterwards, the specimens were saturated by flooding the shearbox external container sheared at displacement rate of 1.6 mm/h. All specimens showed a monotonic increase in shear strength until the ultimate state with compressive behaviour. The specimens from within and outside the failure segment aligned to the same failure envelope in the Mohr-Coulomb plane (Fig. 7) characterised by a friction angle equal to 28.9°.

Probabilistic modelling of hydro-mechanical properties

Material properties have to be characterised in probabilistic terms in order to calculate the probability of failure of the embankment. The experimental characterisation in this study did not provide sufficient data to develop a full probabilistic model for the hydro-mechanical properties of the embankment. The values obtained from the experimental hydro-mechanical characterisation were therefore assumed as mean values, while the standard deviation was estimated on the basis of published values of coefficients of variations COV (ratio of the standard deviation to the mean value) as suggested by Duncan (2000).

- *Friction angle*: COV equal to 13%, in the range 2-13% suggested by Duncan (2000).
- *Saturated hydraulic conductivity*: COV equal to 90%, consistent with literature values ranging from 10% (Nguyen & Chowdhury, 1985) to 160% (Zhang, et al., 2005).
- *Water retention curve:* COV of 60% and 9% were assumed for the α and n parameters in van Genuchten model respectively after Likos et al. (2014). The parameters α and n were assumed to be independent consistently with their physical meaning, being α related to the largest pore size in the material and n to the pore size distribution.

The saturated hydraulic conductivity of the foundation was not considered in probabilistic terms because preliminary studies on the embankment in San Floriano[7] showed that its variability has little influence on the variability of the Factor of Safety. The mechanical properties of the foundation layers do not play any role in the stability analysis because slip surfaces are not deep enough to reach the foundation layers; a deterministic friction angle equal to 33^0 has been assumed for both materials.

A LogNormal distribution was assumed for all variables. Normal or LogNormal distributions are usually selected for the probability distribution of soil hydro-mechanical properties (Arnold

[7] Amabile, A.; Cordão-Neto, M.P.; Pozzato, A.; Tarantino, A. *An accessible approach to assess the probability of failure of flood embankments taking into account transient water flow.* Submitted paper.

& Hicks, 2011), (Suchomel & Mašín, 2010), (Malkawi A.I.H., 2000). The LogNormal distribution has the advantage of never taking any negative values (Uzielli, et al., 2007), which is consistent with most soil properties.

Deterministic assessment of embankment stability

Seepage analysis

The finite element software SEEP/W (GEO-SLOPE, 2004) was used to analyse transient saturated/unsaturated seepage in the embankment and its foundation. The governing equation in SEEP/W is Richards equation (Richards, 1931), which describes two dimensional flow in unsaturated soils as shown in Eq. 3:

$$\frac{\partial}{\partial x}\left(k_x\frac{\partial h}{\partial x}\right)+\frac{\partial}{\partial y}\left(k_y\frac{\partial h}{\partial y}\right)+Q=\frac{\partial \theta}{\partial t} \qquad \textbf{Eq. 3}$$

Where x and y are spatial coordinates, θ is the volumetric water content, h is the hydraulic head, k_x and k_y are a function of θ and represent the hydraulic conductivities in the x and y direction respectively, Q is water flux and t is the time.

The boundary condition on the riverside was represented by the time-dependent hydraulic head (i.e. the hydrograph) recorded during the flood event in 1981, as shown in Fig. 8. The vertical boundary on the landside and the bottom boundary were modelled as impermeable boundaries. The distance of the landside vertical boundary from the toe of the embankment was set equal to 80m, large enough so that the pore-water pressure distribution up to 10 m from the toe of the embankment is not affected by the boundary condition on the landside. The vertical boundary on the riverside is modelled as an impermeable boundary being an axis of symmetry. The crest of the embankment, the landside slope and the ground surface are modelled as potential seepage faces, where pressure can never exceed atmospheric pressure.

The initial condition has been obtained from a steady-state seepage analysis associated with the initial river level for the flood event. In the steady state analysis the far field boundary condition on the vertical boundary on the landside is represented by a constant head equal to 211.45m. This corresponds to the average measurement of water level in a well located 80m from the toe of the embankment observed in winter when the baseline river level was lower than the level in the well. The level in the well was therefore attributed to the far-field groundwater table.

An unstructured mesh of quadrilateral and triangular elements was adopted for the entire domain. The mesh density in the regions where higher gradients develop was optimised by reducing the element size until no significant change in pore-water pressure was observed (~0.5 kPa). For the embankment core, the alluvial deposit and the gravelly shell, elements with size equal to 0.4m were adopted, while 1m elements were used for the lacustrine foundation layer. A constant time step of one hour was used for the entire duration of the seepage simulation (four days). The optimal time step duration was selected with the same approach adopted for the mesh density, by reducing an initial time step of 3 hours until no significant change in pore water pressure was observed (~0.5 kPa).

Stability analysis

The stability analysis was carried out using Bishop's simplified method (Bishop, 1955). The iterative procedure to calculate the Factor of Safety was completed with the software SLOPE/W (GEO-SLOPE, 2004). The pore-water pressures from the transient seepage analysis were used to calculate the evolution of the Factor of Safety over the duration of the flood event. The unsaturated shear strength model (Vanapalli, et al., 1996) implemented by the software was considered appropriate for the embankment coarse-grained material (Tarantino & El Mountassir, 2013). The critical slip surface was assumed circular and then refined with the optimisation algorithm based on the segmental technique.

Probabilistic assessment of embankment stability

The probability of failure of the embankment has been calculated with a probabilistic approach based on the First Order Second Moment (FOSM) method (Wolff, et al., 2004). The Factor of Safety is derived as a Taylor's series expansion with the first order terms of the series used to calculate the mean and variance as a function of the input variables $X_1, \ldots, X_n$. For uncorrelated input variables the mean $\mu[FS]$ and the variance $\sigma^2[FS]$ are given by Eq. 4 and Eq. 5 respectively:

$$\mu[FS] \cong FS(\mu[X_1], \mu[X_2], \ldots, \mu[X_n]) \quad \textbf{Eq. 4}$$

$$\sigma^2[FS] \cong \sum_1^n \left(\frac{\partial FS}{\partial X_i}\right)^2 \sigma^2[X_i] \quad \textbf{Eq. 5}$$

The partial derivatives in Eq. 5 were estimated numerically with a finite difference method by choosing the increment of each input variable equal to its standard deviation. The probability of failure corresponds to the probability of having a Factor of Safety lower than or equal to unity. The application of the FOSM method on its own only provides information about the mean and variance of the Factor of Safety. A probability distribution function of the Factor of Safety must be assumed a priori in order to calculate the probability of failure, very often normal (Baecher & Christian, 2005) or LogNormal (Duncan, 2000). In order to overcome this limitation, the appropriate probability distribution function for the Factor of Safety has been selected with the same approach proposed in Amabile et al.[7]. The selection of the probability distribution function is based on the application of the Monte Carlo method for a single input variable. Different probability distribution functions were fitted to the Monte Carlo-derived empirical distribution function and the Normal distribution function, which returned the best match of the value of the empirical probability of failure, was selected.

Application and results

The number of simulations required for the application of the FOSM method is $2n+1$, where n is the number of independent input variables X_i. Four independent input variables were considered in this study, corresponding to as many material properties (k_{sat}, φ', α, n). In each simulation the minimum value of the Factor of Safety over time FS_m has been obtained[8]. For both cross sections, the minimum Factor of Safety FS_m is fairly linear with respect to the input variables, thus complying with the implicit assumption of the FOSM method that considers only first order terms of the Taylor's series expansion. The mean value of the minimum Factor of Safety $\mu[FS_m]$ corresponds to the result of a deterministic analysis and is associated with the simulation where all input variables are taken with their mean value (Eq. 4). In the remaining $2n$ simulations one variable at a time is increased or decreased by adding or subtracting its standard deviation $\sigma[X_i]$ to its mean value $\mu[X_i]$. The values of minimum Factor of Safety FS_m obtained from these simulations are used to calculate the variance of the minimum Factor of Safety $\sigma^2[FS_m]$ (Eq. 5). The mean and variance of the minimum Factor of Safety FS_m within the failure segment are equal to 1.162 and 0.044 respectively, while outside the failure segment they are equal to 1.631 and 0.112 respectively.

The value of the probability of failure is calculated as the probability to have a Factor of Safety lower than or equal to one and is graphically represented by the shaded areas in Fig. 9. The values of the probability of failure calculated for the section within and outside the failure segment are equal to 22.1% and 2.96% respectively. These values are consistent with the expected probabilities of failure. The probability of failure of the section outside the failure segment is one order of magnitude lower and within the acceptable values reported in the literature for similar cases (Chowdhury, 2010). The probability of failure of the section within

[8] Values in Table S1.

the failure segment, on the other hand, is well outside the acceptable range, thus confirming the validity of the model.

Discussion

Results of the seepage analysis in terms of hydraulic head contours are reported in Fig. 10. Results are shown for the time step corresponding to the peak of the hydrograph in the simulation that resulted in the minimum value of Factor of Safety for both sections. For the section within the failure segment the phreatic surface (bold line in Fig. 10) reaches the ground surface on the toe of the embankment, while for the cross section outside the failure segment positive pore water pressure does not reach the toe of the embankment as the phreatic surface remains below the ground surface by about 0.5m.

The shape of the phreatic surface is also different for the two sections. The phreatic surface lowers down monotonically outside the failure segment whereas it 'bulges' in proximity of the embankment toe within the failure segment. This bulging is due to the upward flow originating from the foundation layer as shown by the velocity vectors in Fig. 10. In turn, this is generated by the sharp contrast in hydraulic conductivity between the alluvial material below the embankment (k=4·10^{-3} m/s) and the lacustrine material on the landside (k=2·10^{-5} m/s). The lacustrine material acts as a barrier diverting the water flow upward towards the embankment toe. On the other hand, water flow is not diverted in the section outside the failure segment because there is no contrast in hydraulic conductivity in the horizontal direction.

The different water flow pattern affects the distribution of hydraulic head at the embankment toe. In the failure segment, hydraulic head is not dissipated in the alluvial material below the embankment because its hydraulic conductivity is much higher than the adjacent lacustrine deposit. This makes available the full hydraulic head at the base of the embankment and water flow therefore occurs upwards with relatively high hydraulic gradients. This does not occur outside the failure segment as the hydraulic head dissipates uniformly in the homogenous alluvial deposit.

In turn, the different distribution of hydraulic head and, hence, pore-water pressures affect the stability of the embankment. In the section within the failure zone, the build-up of pore water pressure at the toe of the embankment leads to decrease in the shear strength and lower Factor of Safety. Results of the stability analysis resulting in the minimum Factor of Safety FS_m are shown in Fig. 11.

The critical slip surface obtained in the mean value (deterministic) simulation has been considered in all the other simulations (Phoon, 2008). Its shape and position compare very favourably with the scarp observed during the flood in 1981, when a cut of about 50 cm of depth was observed on the crest of the embankment.

The variation of Factor of Safety over time for the mean value simulation is shown in Fig. 12. The minimum Factor of Safety FS_m is not attained at the same time in both sections. It corresponds to the time of maximum river level (t = 1.125 days) for the section within the failure segment and t = 1.500 days for the section outside the failure segment. This can be explained by the results of the seepage analysis. The Factor of Safety depends on the value of the pore water pressure along the slip surface. In the section within the failure segment the variation of pore water pressure is immediately affected by the variation of river level because of the high hydraulic transmissivity of the confined alluvial layer beneath the embankment. This is shown by the fact that the maximum pore water pressure for a point at a depth of 0.5 m below the toe of the embankment corresponds to the peak of the hydrograph (Fig. 12). In the section outside the failure segment pore water pressure along the slip surface is less affected by variations in river level, even if the foundation material is extremely permeable, because water tends to flow towards the landside. The value of pore water pressure along the slip surface increases more slowly because water flow is taking place in the embankment from the river, not from the foundation layer, therefore the seepage process is governed by the hydraulic conductivity of the unsaturated embankment material. For this reason it takes some time for the water front to reach the slip surface, resulting in a delay between the peak of the hydrograph and the time when the maximum pore water pressure and, hence, the minimum Factor of Safety is attained.

The conclusion drawn by this comparison is that the stability of the embankment is strongly affected by the water flow regime, which is in turn strongly controlled by the hydraulic conductivity of the material on the landside of the embankment (and not just by the hydraulic conductivity of the material directly beneath the embankment). In the section outside the failure segment the presence of a permeable foundation layer on its own is not a decisive cause for the development of uplift pressure.

These findings seem to be consistent with previous literature. Seed et al. (2008) emphasized the key role played by the soil profile beneath the toe of the North London Canal embankment in New Orleans when comparing the behaviour of two sections with very similar soil profiles. Although both embankments were built on very permeable foundation layers, only one of them collapsed during Hurricane Katrina. Their results highlighted that a subtle difference in soil profile even beyond the toe of the embankment can have catastrophic consequences in terms of embankment stability. The results presented in this work about the case study of the Adige River embankment confirm that instability triggered by uplift pressures is a complex failure mechanism and the critical role played by the foundation material on the landside cannot be adequately captured by approaches that assume horizontally layered soil profiles.

Conclusions

The paper has presented the case study of the embankment instability along the Adige River. A segment of this embankment experienced instability in the form of a scarp without collapsing, thus offering the chance to investigate soil profile and material properties as they were at the time of instability. Soil profile within and outside the failure segment has been inferred from boreholes, DPH tests and EM scanning. The hydro-mechanical properties of the embankment and its foundation have been characterised through laboratory tests and inverse analysis of water flow based on field measurements below and above phreatic surface.

The hydro-mechanical model has been validated by calculating the probability of failure within and outside the failure segment with a FOSM-based approach. The calculated probability of failure has shown a good agreement with the expected probability of failure for the sections within and outside the failure segment.

The analysis of the flow regime within the segment that experienced failure has shown that the contrast in hydraulic conductivity in the foundation layers on the landside leads to an upward diversion in the water flow and build-up of pore-water pressures at the toe of the embankment. On the other hand, the zone outside the failure segment is characterised by homogeneous foundation layers and the water flow towards the landside is undisturbed, with dissipation of hydraulic head taking place in horizontal direction in the foundation layers beneath the embankment and on the landside.

These results show that the high hydraulic conductivity of the foundation layer does not represent per se a critical condition for the development of uplift pressures at the toe of the embankment. The material outside the embankment footprint can play indeed a key role on the water flow regime and, hence, on the stability of flood embankments. The role of the soil profile on the landside is often overlooked and should be addressed by site investigation.

Acknowledgements

The authors wish to acknowledge the support of the European Commission via the Marie Curie IEF project RESCUE 'River flood Embankments Subject to Climate change: Understanding Effects of future floods and novel 'low-carbon' adaptation measures' (PIEF-GA-2013-625258) and the Marie Curie Industry-Academia Partnership and Pathways Network MAGIC ‘Monitoring systems to Assess Geotechnical Infrastructure subjected to Climatic hazards’ (PIAPP-GA-2012-324426). The authors also wish to acknowledge the support of the Autonomous Province of Bolzano (Italy).

Supplemental data

Supplemental data are provided in the attached file.

References

Aldegheri, A., 2009. *Instabilità degli Argini Fluviali: il Caso di S. Floriano (BZ).* s.l.:Università degli Studi di Trento.

Amabile, A., Cordão-Neto, M., De Polo, F. & Tarantino, A., 2016. *Reliability analysis of flood embankments taking into account a stochastic distribution of hydraulic loading.* Paris, Proceedings of 3rd European Conference on Unsaturated Soils .

Amabile, A., Cordão-Neto, M., Pozzato, A. & Tarantino, A., Glasgow, UK. An accessible approach to assess the probability of failure of flood embankments taking into account transient water flow. *Working paper.*

Angelucci, D., 2013. *La valle dell'Adige: genesi e modificazione di una grande valle alpina come interazione tra dinamiche naturali e fattori antropici. Conference: Il fiume, le terre, l'immaginario. L'Adige come fenomeno storiografico complesso.* Rovereto, V. Rovigo.

Arnold, P. & Hicks, M., 2011. *A stochastic approach to rainfall-induced slope failure, in Proceedings of the 3rd International Symposium on Geotechnical Safety and Risk.* Munich, Karlsruhe, Germany, Bundesanstalt für Wasserbau.

Baecher, G. & Christian, J., 2005. *Reliability and Statistics in Geotechnical Engineering.* s.l.:John Wiley & Sons.

Bauduin, C. M. H., Moes, C. J. B. & Van Baalen, M., 1989. The influence of uplift water pressures on the deformations and stability of flood embankments. In: *Proceedings of the 12th International Conf. Soil Mechanics Foundation Engineering.* Rio de Janeiro, Brazil: s.n., p. 1713–1716.

Bishop, A., 1955. The use of the Slip Circle in the Stability Analysis of Slopes. *Géotechnique,* 5(1), pp. 7-17.

Chowdhury, R., 2010. *Geotechnical slope analysis.* London, UK: Taylor and Francis.

CIRIA; French Ministry of Ecology; USACE, 2013. *The International Levee Handbook.* London: Ciria.

Cooling, L. & Marsland, A., 1953. Soil Mechanics Studies of Failures in the Sea Defence Banks of Essex and Kent. In: *Conference on the North Sea Floods of 31st January–1st February.* London: The Institution of Civil Engineers, pp. 58-73.

Duncan, J., 2000. Factors of Safety and reliability in geotechnical engineering. *J. Geotech. Geoenviron. Eng.,* 126(4), pp. 307-316.

Dyer, M., 2004. Performance of flood embankments in England and Wales. *Proceedings of the Institution of Civil Engineers,* Water Management 157(Issue WM4), pp. 177-186.

EN 1997-2, 2007. *Eurocode 7 - Geotechnical design - Part 2: Ground investigation and Testing,* s.l.: s.n.

GEO-SLOPE, 2004. *Seepage Modeling with SEEP/W.* s.l.:GEO-SLOPE International, Ltd..

GEO-SLOPE, 2004. *Stability Modeling with SLOPE/W.* s.l.:GEO-SLOPE International Ltd. .

Herzog, B. & Morse, W., 1986. Hydraulic conductivity at a hazardous waste disposal site: comparison of laboratory and field determined values. *Waste Management and Research,* Volume 4, pp. 177-187.

Hird, C., Marsland, A. & Schofields, A., 1978. The development of centrifugal models to study the influence of uplift pressures on the stability of a flood bank. *Geotechnique,* 28(1), pp. 85-106.

Kanning, W., Baars, S. V. & Vrijling, J. K., 2008. *The Stability of Flood Defenses on Permeable Soils: The London Avenue Canal.* Arlington, VA, International Conference on Case Histories in Geotechnical Engineering.

Lambe, T. & Whitman, R., 1969. *Soil Mechanics.* s.l.:Wiley.

Lancellotta, R., 2009. *Geotechnical Engineering.* Second Edition ed. s.l.:Taylor and Francis.

Likos, W., Lu, N. & Godt, J., 2014. Hysteresis and Uncertainty in Soil Water-Retention Curve Parameters. *J. Geotech. Geoenviron. Eng.,* 140(4).

Malkawi A.I.H., H. W. A. F., 2000. Uncertainty and reliability analysis applied to slope stability. *Structural Safety,* Volume 22, pp. 161-187.

Marsland, A. & Randolph, M., 1978. A study of the variation and effects of water pressures in the pervious strata underlying Crayford Marshes. *Géotechnique,* 28(4), pp. 435-464.

Nabighian, M., 1992. *Electromagnetic Methods in Applied Geophysics, Volume 2.* Denver, Colorado, US: Newmont Exploration Limited.

Nguyen, V. & Chowdhury, R., 1985. Simulation for risk analysis with correlated variables. *Géotechnique,* 35(1), pp. 47-58.

Phoon, K., 2008. *Reliability-Based Design in Geotechnical Engineering. Computations and Applications.* s.l.:Taylor & Francis.

Pozzato, A., 2009. *Stability of river embankment of coarse-grained well-graded soil: the case study of the Adige river at Egna (BZ).* s.l.:Università degli Studi di Trento.

Pozzato, A., Tarantino, A. & De Polo, F., 2014. Analysis of the effects of the partial saturation on the Adige river embankment stability. In: *Unsaturated Soils: Research & Applications.* Sydney, Australia: s.n., pp. 1367--1372.

Richards, L., 1931. Capillary Conduction of Liquids Through Porous Mediums. *Physics,* Volume 1.

Seed, R. et al., 2008. New Orleans and Hurricane Katrina. I: Introduction, Overview, and the East Flank. *Journal of Geotechnical and Geoenvironmental Engineering,* 134(5), pp. 701-717.

Seed, R. et al., 2008. New Orleans and Hurricane Katrina. IV: Orleans East Bank (Metro) Protected Basin. *Journal of Geotechnical and Geoenvironmental Engineering,* 134(5), pp. 762-779.

Simeoni, L., Zatelli, P. & Floretta, C., 2014. Field measurements in river embankments: validation and management with spatial database and webGIS. *Nat Hazards,* Volume 71, p. 1453–1473.

Suchomel, R. & Mašín, D., 2010. Comparison of different probabilistic methods for predicting stability of a slope in spatially variable c–u soil. *Computers and Geotechnics,* Volume 37, pp. 132-140.

Tarantino, A. & El Mountassir, G., 2013. Making unsaturated soil mechanics accessible for engineers: preliminary hydraulic-mechanical characterisation and stability assessment. *Engineering Geology,* Volume 165, pp. 89-104.

Tarantino, A. & Mongiovì, L., 2003. Calibration of tensiometer for direct measurement of matric suction. Technical Note.. *Géotechnique,* 53(1), pp. 137-141.

Tarantino, A. & Tombolato, S., 2005. Coupling of hydraulic and mechanical behaviour in unsaturated compacted clay. *Géotechnique,* 55(4), pp. 307-317.

Uzielli, M., Lacasse, S., Nadim, F. & Phoon, K., 2007. Soil variability analysis for geotechnical practice. In: *Characterisation and Engineering Properties of Natural Soils.* s.l.:Taylor & Francis Group, pp. 1653-1754.

van Genuchten, M., 1980. A Closed-form Equation for Predicting the Hydraulic Conductivity of Unsaturated Soils. *Soil Sci. Soc. Am. J.,* Volume 44, pp. 892-898.

Vanapalli, S., Fredlund, D., Pufahl, D. & Clifton, A., 1996. Model for the prediction of shear strength with respect to soil suction. *Can. Geotech. J.,* Volume 33, pp. 379-392.

Van, M., Koelewijn, A. R. & Barends, F., 2005. Uplift Phenomenon: Model, Validation, and Design. *International Journal of Geomechanics,* 5(2), pp. 98-106.

Werth, K., 2003. *Geschichte der Etsch: zwischen Meran und San Michele Flussregulierung, Trockenlegung der Möser, Hochwasserschutz.* s.l.:Tappeiner.

Wolff, T. et al., 2004. *Geotechnical Reliability of Dam and Levee Embankments,* s.l.: U.S. Army Corps of Engineers.

Zhang, L., Zhang, L. & Tang, W., 2005. Rainfall-induced slope failure considering variability of soil properties. *Géotechnique,* 55(2), pp. 183-188.

Zwanenburg, C. et al., s.d. Lessons learned from dike failures in the past decades. *International Journal of Geoengineering Case histories,* Volume Submitted 2017.

Captions of Figures

Fig. 1. Ancient meanders of the riverbed before the construction of flood embankments (Werth, 2003).

Fig. 2. Longitudinal soil profile: layer boundaries identified from visual inspection of the borehole logs (diamonds) and DPH tests (circles), samples collected for grain size analysis (black rectangles) and studied sections within and outside the failure segment (dashed lines).

Fig. 3. EM measurements along the longitudinal profile taken on the landside at the toe of the embankment.

Fig. 4. Soil profile for the section within (left) and outside (right) the failure segment.

Fig. 5. Grain size distributions for (a) embankment core, (b) alluvial deposit, (c) lacustrine deposit (grey = samples within failure segment; white = samples outside failure segment).

Fig. 6. Comparison between measured (continuous lines) and simulated (dashed lines) values of (a) pore water pressure in tensiometers and (b) hydraulic head in piezometers.

Fig. 7. Failure envelope obtained from direct shear tests on two sets of specimens from the embankment core.

Fig. 8. Hydrograph recorded during the flood event in 1981.

Fig. 9. Probability of failure for the sections within and outside the failure segment.

Fig. 10. Hydraulic head contours and water flow vectors in the transient seepage analysis for the sections within (left) and outside (right) the failure segment at the time of peak.

Fig. 11. Critical slip surface and minimum value of the Factor of Safety FS_m for the sections within (left) and outside (right) the failure segment.

Fig. 12. Variation over time of Factor of Safety and pore water pressure at the toe of the embankment (depth = 0.5 m) compared to flood hydrograph.

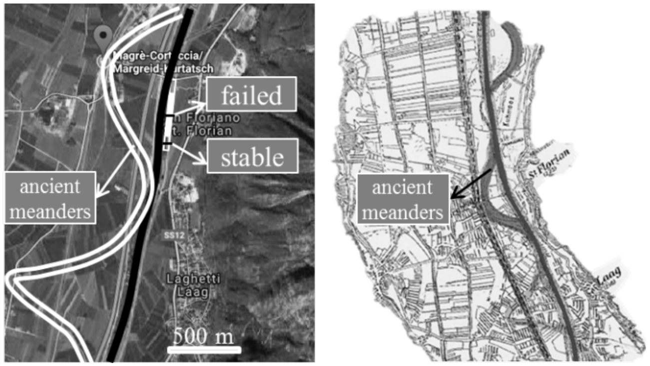

Fig. 1. Ancient meanders of the riverbed before the construction of flood embankments (Werth, 2003).

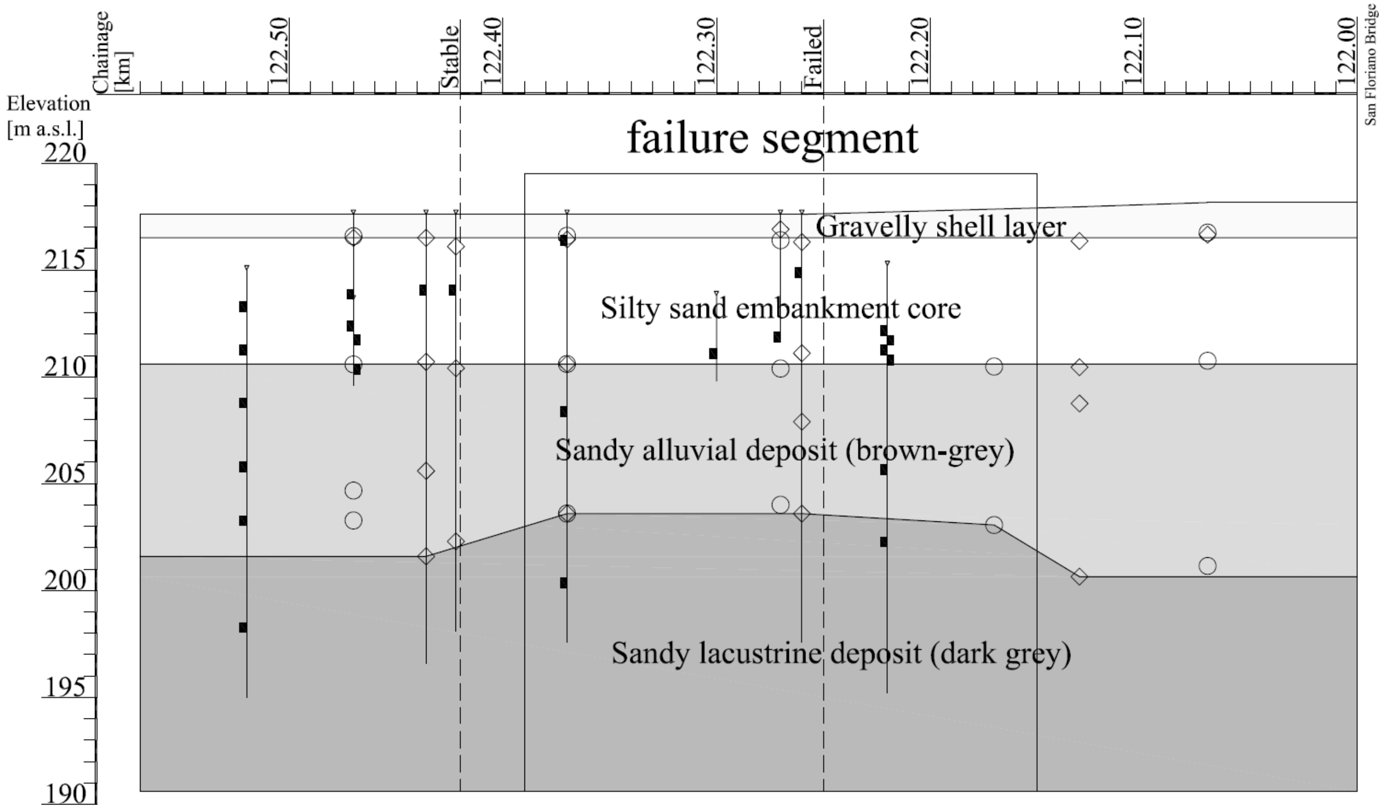

Fig. 2. Longitudinal soil profile: layer boundaries identified from visual inspection of the borehole logs (diamonds) and DPH tests (circles), samples collected for grain size analysis (black rectangles) and studied sections within and outside the failure segment (dashed lines).

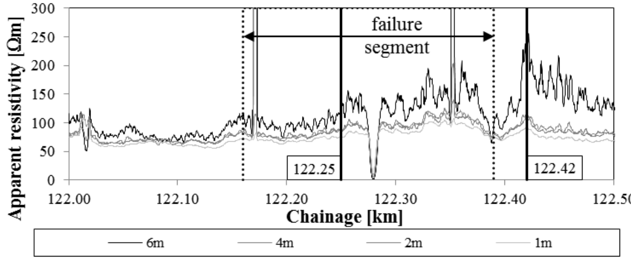

Fig. 3. EM measurements along the longitudinal profile taken on the landside at the toe of the embankment.

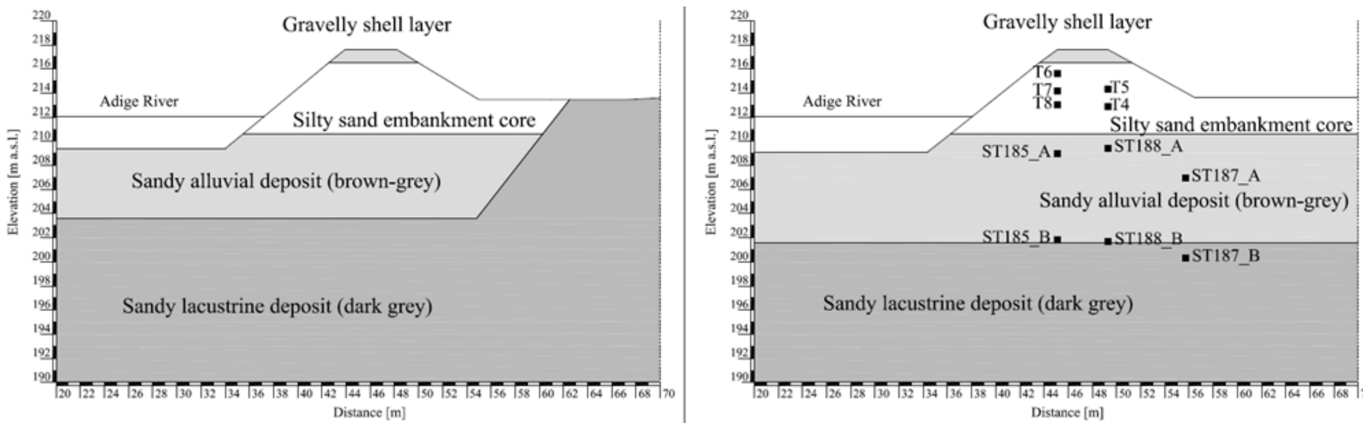

Fig. 4. Soil profile for the section within (left) and outside (right) the failure segment.

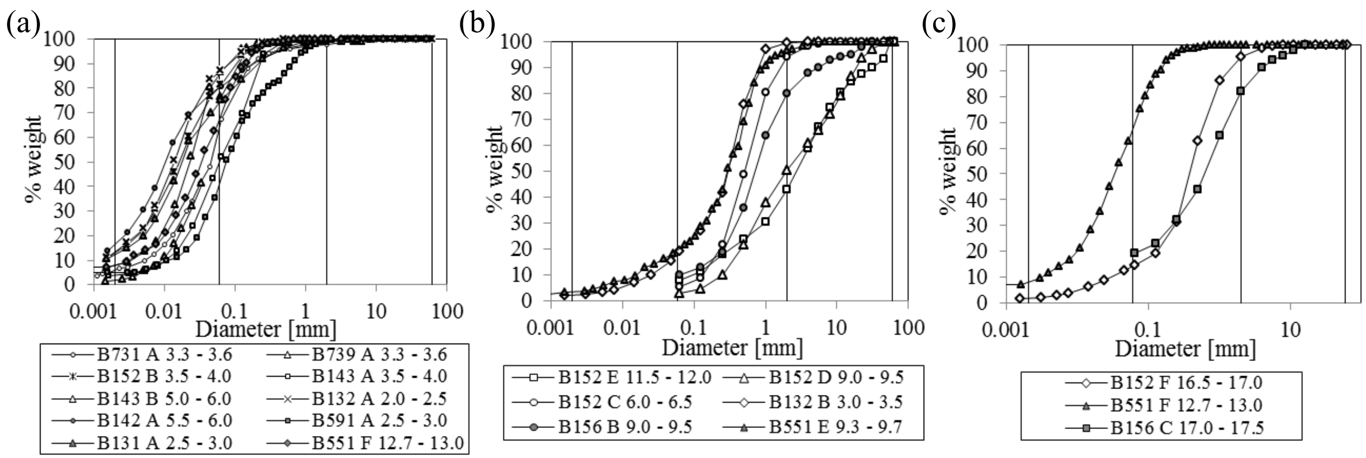

Fig. 5. Grain size distributions for (a) embankment core, (b) alluvial deposit, (c) lacustrine deposit (grey = samples within failure segment; white = samples outside failure segment).

(a)

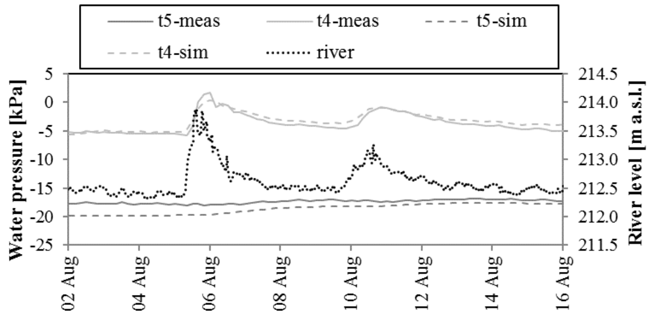

(b)

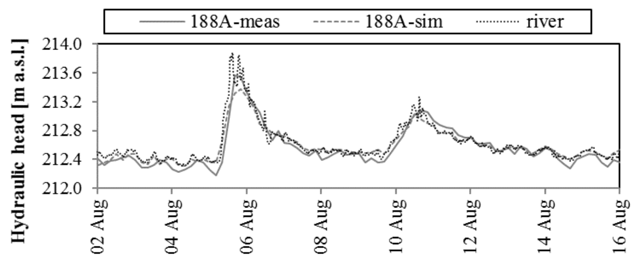

Fig. 6. Comparison between measured (continuous lines) and simulated (dashed lines) values of (a) pore water pressure in tensiometers and (b) hydraulic head in piezometers.

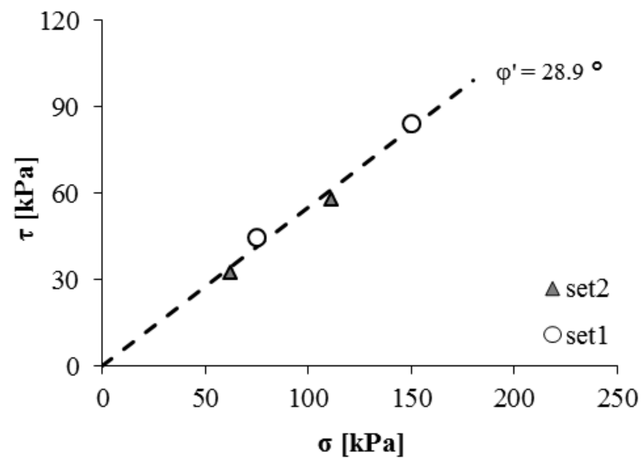

Fig. 7. Failure envelope obtained from direct shear tests on two sets of specimens from the embankment core.

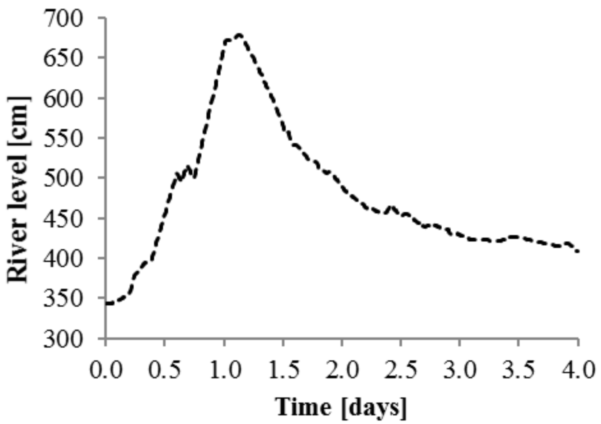

Fig. 8. Hydrograph recorded during the flood event in 1981.

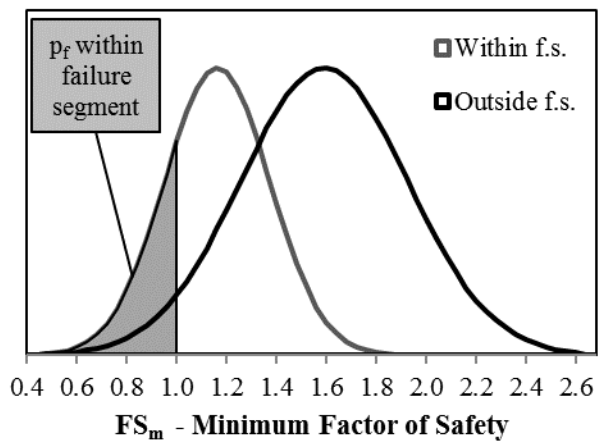

Fig. 9. Probability of failure for the sections within and outside the failure segment.

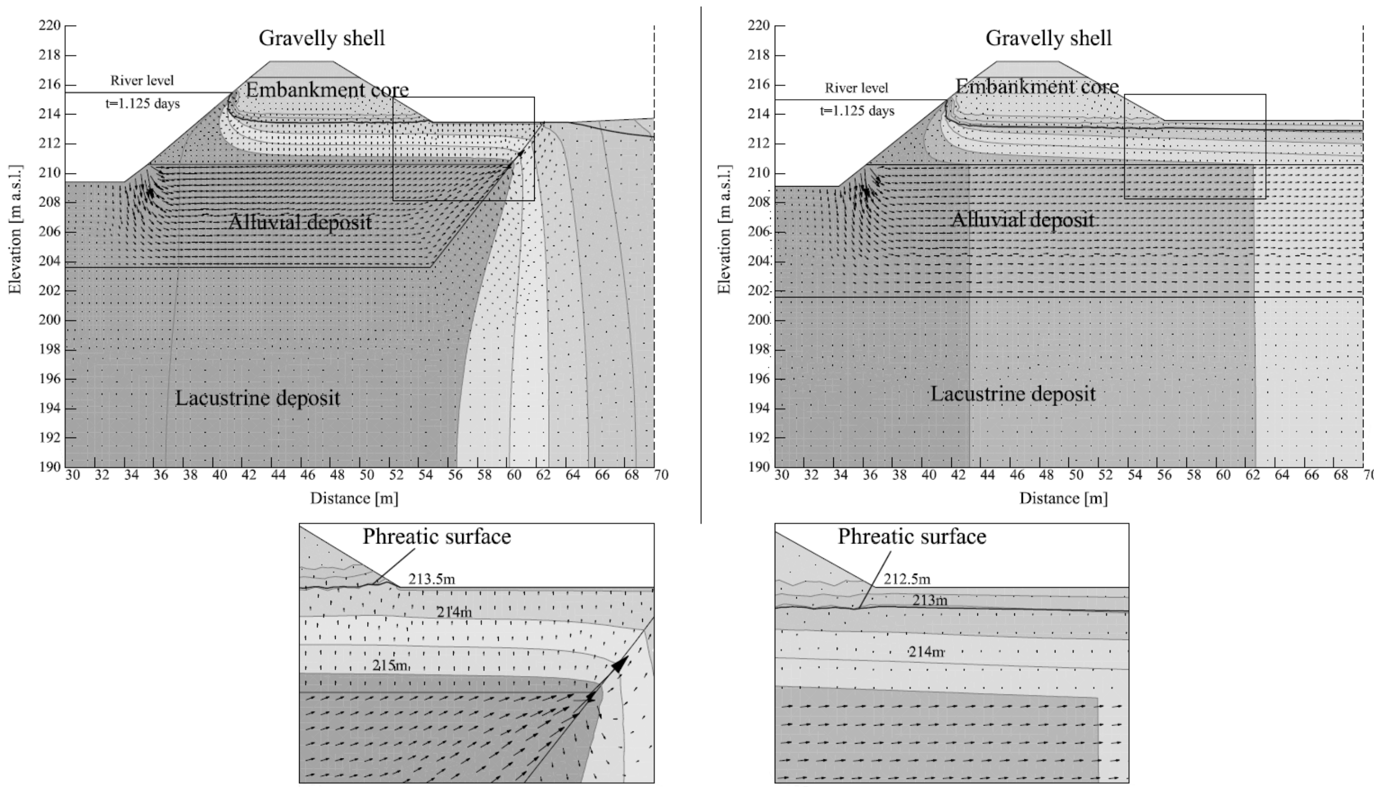

Fig. 10. Hydraulic head contours and water flow vectors in the transient seepage analysis for the sections within (left) and outside (right) the failure segment at the time of peak.

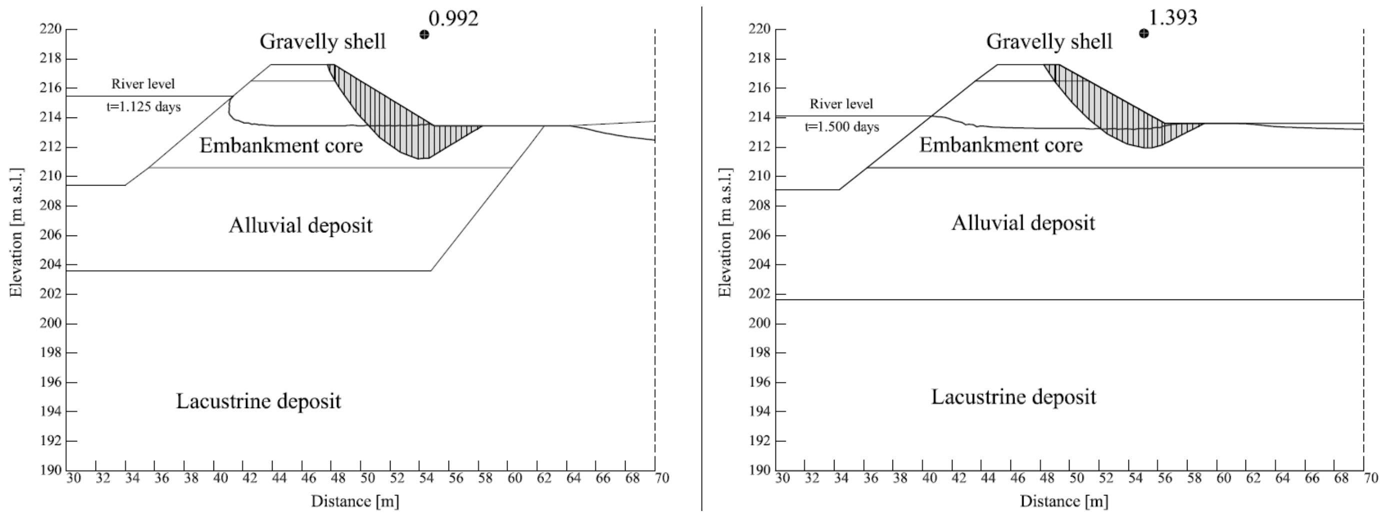

Fig. 11. Critical slip surface and minimum value of the Factor of Safety FS_m for the sections within (left) and outside (right) the failure segment.

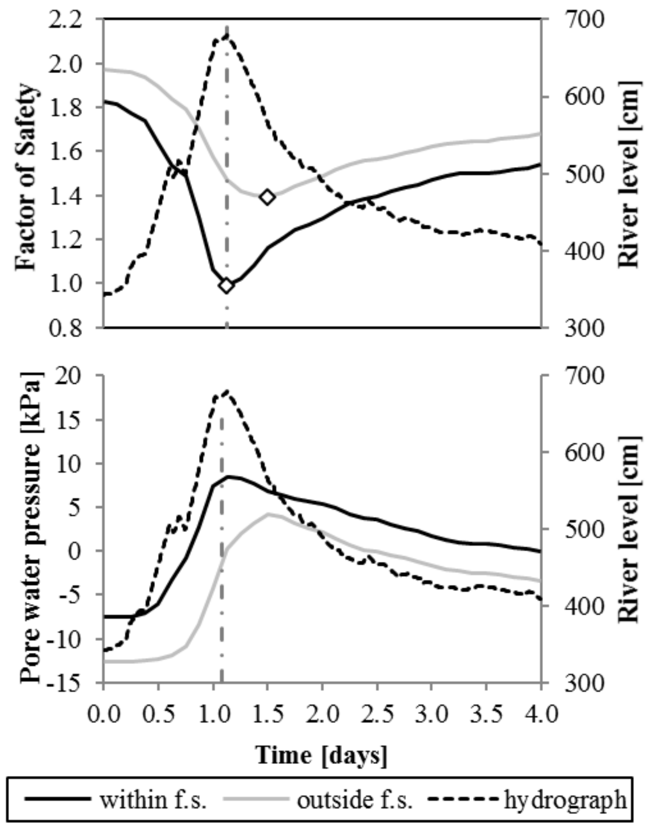

Fig. 12. Variation over time of Factor of Safety and pore water pressure at the toe of the embankment (depth = 0.5 m) compared to flood hydrograph.